CONTROL DESIGN FOR CANCELLATION OF UNNATURAL REACTION TORQUE AND VIBRATIONS IN VARIABLE-GEAR-RATIO STEERING SYSTEM

Atsushi Oshima
Mechatronics Development Center
NSK Ltd,
Fujisawa, Kanagawa Japan 251-8501
Email: oshima-a@nsk.com

Xu Chen
Department of Mechanical Engineering
University of California, Berkeley
Berkeley, California 94720
Email: maxchen@me.berkeley.edu

Sumio Sugita
Mechatronics Development Center
NSK Ltd,
Fujisawa, Kanagawa Japan 251-8501
Email: sugita-s@nsk.com

Masayoshi Tomizuka
Department of Mechanical Engineering
University of California, Berkeley
Berkeley, California 94720
Email: tomizuka@me.berkeley.edu

ABSTRACT

Variable-gear-ratio steering is an advanced feature in automotive vehicles. As the name suggest, it changes the steering gear ratio depending on the speed of the vehicle. This feature can simplify steering for the driver, which leads to various advantages, such as improved vehicle comfort, stability, and safety. One serious problem, however, is that the variable-gear-ratio system generates unnatural torque to the driver whenever the variable-gear-ratio control is activated. Such unnatural torque includes both low-frequency and steering-speed-dependent components. This paper proposes a control method to cancel this unnatural torque. We address the problem by using a tire sensor and a set of feedback and feedforward algorithms. Effectiveness of the proposed method is experimentally verified using a hardware-in-the-loop experimental setup. Stability and robustness under model uncertainties are evaluated.

INTRODUCTION

Variable-gear-ratio steering is a speed-dependent steering system. This steering mechanism includes a variable actuator which controls the relative angle between the steering wheel and the tire [1]. The ability to vary the steering gear ratio brings various advantages. For instance, the steering gear ratio is set to be high when the vehicle speed is low. This allows a small steering-wheel motion to provide a large steering angle, which is desirable in situations such as parking. On the other hand, at high speeds, a smaller steering gear ratio can be used, therefore enhancing vehicle stability in situations such as freeway driving.

A serious problem of this advanced steering system is that unexpected torque is relayed to the driver whenever the variable-gear-ratio control is activated [2,3]. More specifically, when the variable actuator changes the steering gear ratio, a reaction torque from the motor is transmitted up the steering column, which is felt by the driver as an unnatural torque.

In past works, the authors in [2,3] decoupled the gear-ratio control and the torque-assist control in an attempt to mitigate this unnatural reaction torque. This design, however, requires an accurate system model and an estimate of the tire force. In an alternative approach, the authors in [1] proposed friction relocation control to reduce the unnaturalness in variable-gear-ratio steering systems. This method uses a fictitious torque-absorbing control function which reduces the unnaturalness between the driver and the variable actuator. This approach relies on model-based feedforward control, hence its performance is highly sensitive to model uncertainties.

This paper proposes a control scheme which not only mitigates the unnatural reaction torque, but also improves the servo performance of the overall Electrical Power Steering (EPS) system. We first propose a velocity feedback controller to reduce the unnatural torque, and then introduce two additional controllers with a tire sensor to maintain the desired normal steering function. Since the steering performance is additionally affected by friction and narrow-band disturbances generated by the EPS motor, a friction compensator and a narrow-band disturbance observer (DOB) in the presence of system delays are also introduced. Lastly, the stability and robustness of the proposed controller in the presence of model

uncertainties will be evaluated by the structured singular value analysis. The effectiveness of the overall control scheme is then validated though experiments on a hardware-in-the-loop simulator.

VARIABLE-GEAR-RATIO STEERING

Fig. 1 shows a schematic diagram of the variable-gear-ratio steering system. A variable actuator is installed between the steering wheel and the torsion spring. The actuator controls the relative angle $\Delta\theta$ between the steering wheel θ_w and the steering shaft θ_s.

$$\Delta\theta \equiv \theta_w - \theta_s \tag{1}$$

Denote α as the gear-ratio command and θ_p as the pinion angle. Let $\Delta\theta$ be given by

$$\Delta\theta = \theta_p(-1 + 1/\alpha) \tag{2}$$

It is assumed that the pinion angle θ_p and the steering shaft angle θ_s remain close to each other ($\theta_p \approx \theta_s$). Under this assumption, the system behaves as if a gear-ratio transmission is added between θ_p and θ_w:

$$\theta_p = \alpha\theta_w \tag{3}$$

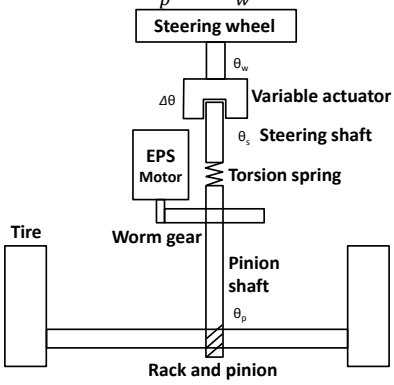

FIGURE 1. VRIABLE-GEAR-RATIO STEERING

To understand the occurrence of the unnatural reaction torque, suppose that a command is given to change $\Delta\theta$ from zero to one radian. The actuator needs to generate torque to cause this change. As a consequence, a reaction torque will be transmitted to the steering wheel, since the output shaft of the actuator is connected to the steering shaft and the casing of the actuator is connected to the steering wheel (see Fig. 1).

SYSTEM MODELING

Fig. 2 shows a simplified model of the variable-gear-ratio steering system. The variable actuator has a built-in controller which yields a very high closed-loop bandwidth; hence the dynamics of the variable actuator can be ignored in the analysis. V_v, the actuator velocity at the second input node, therefore is equivalent to $\Delta\dot{\theta}$, and is measured by an encoder.

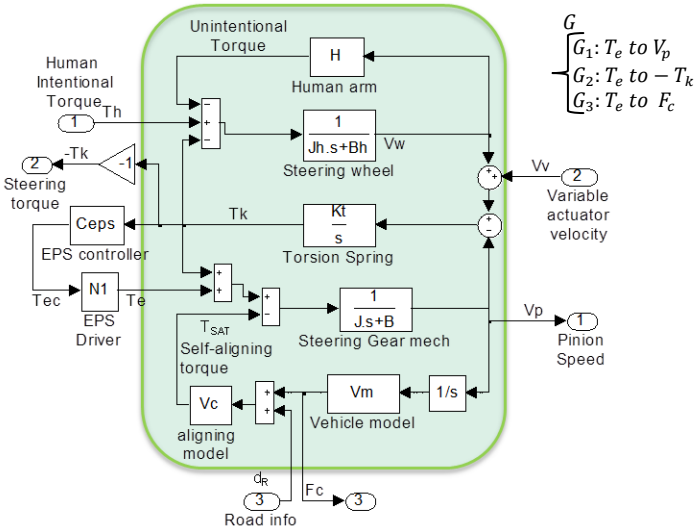

FIGURE 2. SYSTEM MODELING

Overall, we have:

(i), the signals of the three input nodes: T_h, V_v and d_R are the external inputs from the human, the variable actuator, and the road, respectively;

(ii), the measurements of the system: V_p, T_k, and F_c are the pinion speed (which is equivalent to the speed of the EPS motor), the steering torque detected by the torsion-spring deflection, and the tire force detected by the tire-force sensor respectively.

H is a model of the human arm. When the human driver grasps the steering wheel, the resonance frequency of the steering system significantly changes. H is experimentally obtained as follows: isolate the steering wheel by cutting the physical connection between the steering wheel and the torsion bar; excite the steering wheel by motor, i.e. apply the excitation signal at T_h (Human Intentional Torque) in Fig, 2; identify the dynamics from T_h to V_w twice, once with and the other without the human grasping the steering wheel; and finally obtain H from the two identified models by considering the feedback connection between H and $1/(J_hs+B_h)$. In the two blocks named "steering wheel" and "steering gear mech", J and J_h are the inertias of the steering gear and the steering wheel respectively; B and B_h are the corresponding damping coefficients. In the torsion spring block, K_t is the spring constant. V_m (near the third output node) is the vehicle model whose input is the pinion angle and the output is the tire force. This block assumes a vehicle-speed-dependent second-order model [10]. V_c is the aligning model that explains the relationship between the tire force and the self-aligning torque T_{SAT}.

The components described above are combined to form the (green) box in Fig. 2, which represents the mechanical plant of the EPS system. Outside the plant, N_1 represents the EPS driver and the signal processing unit. It can be modeled as a delay

element. The EPS controller C_{eps} and N_1 can be thought as the controller element for the EPS hardware. The effects of T_e to the system output can be modeled by a single-input-multi-output (SIMO) plant given as $G = [G_1, G_2, G_3]^T$, where G_1, G_2, G_3 are transfer functions from T_e to $V_p, -T_k$, and F_c respectively.

FEEDBACK CONTROL STRUCTURE FOR CANCELLING THE UNNATURAL TORQUE

Desired conditions

The goal of the feedback controller is to suppress the unnatural torque caused by the EPS motor. Due to safety reasons, however, torque feedback caused by road conditions must still reach the driver. The list of conditions that the closed-loop EPS system must achieve is summarized below:

1. The velocity of the variable actuator does not affect the steering torque;
2. The original operability of the steering wheel is preserved;
3. The road condition is normally transmitted to the driver.

The first condition ensures that the unnatural torque caused by the EPS motor is mitigated. The second and third conditions are needed to ensure that EPS system still retains its regular steering function. Three separate controllers are proposed to help satisfy these conditions.

Controller C_1 for unnatural-torque cancellation

Recall that G_1 represents dynamics between the EPS output torque T_e and the pinion speed V_p. Controller C_1 in Fig. 3 is a PID controller that uses high-gain control to achieve the first desired condition. From Fig. 4, if the output signal V_p of this feedback loop is almost equal to V_v, the transfer function from V_v to V_p is approximately one (at low frequencies). As a result, the transfer function from V_v to T_k is approximately zero. Thus changes in $\Delta\theta$ by the variable-gear-ratio mechanism do not transmit any additional torque to the driver.

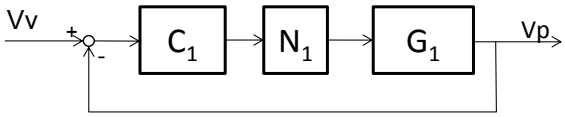

FIGURE 3. FEEDBACK CONTROLLER

EPS assistive controller C_2

Controller C_1 affects the characteristic of EPS assistive torque. Controller C_2 is proposed to satisfy the second desired condition. This is a feedforward controller in the form $C_2 = C_{eps}G_{1n}$, where C_{eps} is the original EPS controller and G_{1n} is the nominal plant model. If Controller C_1 realizes good tracking control in the velocity control loop in Fig. 3, then the transfer function from T_k to V_p in Fig. 5 is approximately $C_2 \approx C_{eps}G_1$, namely, the original operational relationship between T_k and V_p are preserved.

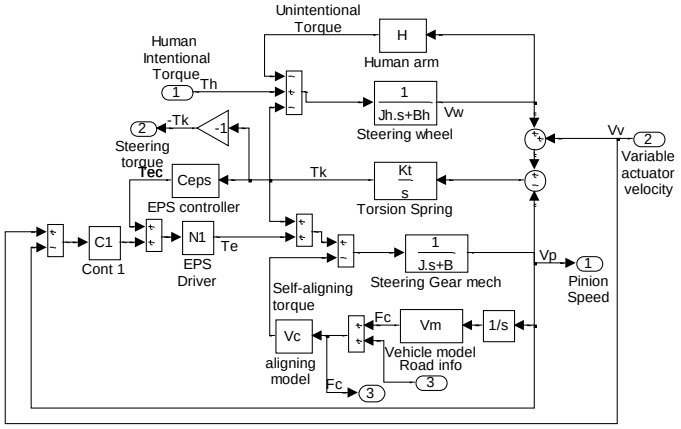

FIGURE 4. FEEDBACK CONTROL STRUCTURE

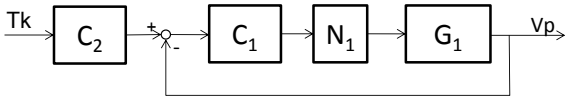

FIGURE 5. EPS ASSISTIVE CONTROLLER C_2

Controller C_3 for transmitting road information

In the original EPS system, the transfer function between d_R and V_p is $-V_cG_1$. If controller C_1 is added, the transfer function from d_R to V_p becomes $-V_cG_1/(1 + C_1G_1N_1)$, which has low gains at low frequencies since $G_1/(1 + C_1G_1N_1)$ is the input disturbance rejection function in Fig. 3. In addition, the frequency range of V_v and that of the necessary road information d_R (for example, friction between the tires and the road) mostly overlap, both at around 0-10 Hz. Hence while realizing good tracking control between V_v and V_p, controller C_1 also rejects the road information d_R. Controller C_3 is then proposed to satisfy the third desired condition. To transmit the road condition, a tire sensor may be used to obtain the self-aligning torque. In this paper a NSK multi sensing hub unit [4], which is currently under industrial development, is used to measure the tire force F_t. It is converted to T_{SAT} using the relationship $T_{SAT} = V_cF_t$. Modeling V_c is in itself a rich research field [7,8] and is beyond the scope of this paper. We will assume V_c is a constant in the remainder of the analysis.

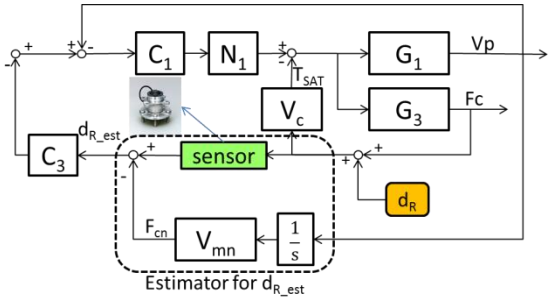

FIGURE 6. STRUCTURE OF CONTROLLER C_3

C_3 is proposed to be $C_3 = V_{cn}G_{1n}$, where V_{cn} is the nominal aligning model. As shown in Fig. 6, the input to C_3 is the estimate of the road information, d_{R_est}, which is obtained by subtracting the estimated Fc from the sensor output. Additionally, the transfer function from d_{R_est} to V_p is $-C_3C_1G_1N_1/(1+C_1G_1N_1)$, which approximately equals $C_3 = V_{cn}G_{1n} \approx V_cG_1$ at low frequencies, since $C_1G_1N_1/(1+C_1G_1N_1)$ is the transfer function between V_v and V_p in Fig. 3. Recall that $-V_cG_1$ is the original closed-loop transfer function between d_R and V_p; Controller C_3 hence achieves the third desired condition.

Summary

Fig. 7 shows the overall system with controllers C_1, C_2, C_3. These controllers are designed to satisfy the three desired conditions if C_1 realizes perfect tracking control in the velocity loop in Fig. 3.

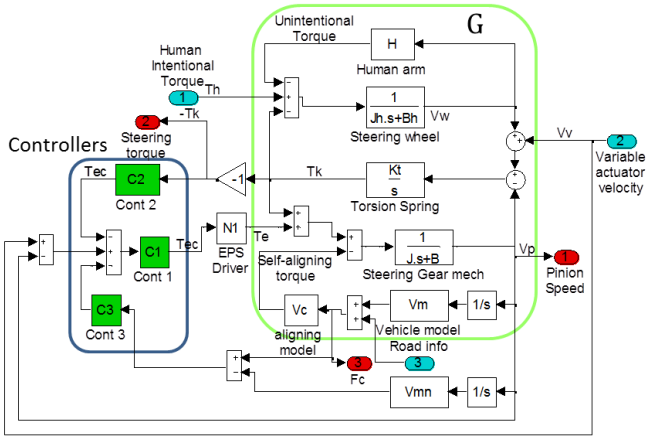

FIGURE 7. OVERALL SYSTEM WITH C_1, C_2, C_3

INITIAL EXPERIMENTAL RESULTS

Experimental setup

Fig. 8 shows the variable actuator installed in the experimental setup. It is constructed by a combination of a harmonic gear and a DC brushless motor. The control algorithm is evaluated on the hardware-in-the-loop (HIL) simulator. The real-time operation environment is realized by National Instruments' LabVIEW Real-Time for ETS targets. The variable-actuator controller, the EPS controller, and the vehicle model operate at a 1-ms sampling period. The plant is developed and implemented with a 4-DOF (X, Y, yaw, roll) vehicle model and a nonlinear tire model. The calculated tire force in the model and the self-aligning torque are fed back to the reaction motor to obtain realistic steering reaction torques.

Evaluation of unnatural torque cancellation

This section will evaluate the controllers' performance in achieving the first desired condition, namely rejecting the unnatural torque caused by the EPS system. Fig. 9(a) plots the steering torque produced by the normal EPS controller, and Fig. 9(b) plots the result when controllers C_1 and C_2 are applied. In both plots, the variable-gear-ratio steering is giving a sinusoidal command of $\alpha = 1 + 0.3\sin(1.6\pi t)$ while the steering wheel is kept at a fixed 30-deg position by the driver. Throughout this experiment, the vehicle model in the real-time experimental setup is running at 50km/h on a dry and clear road.

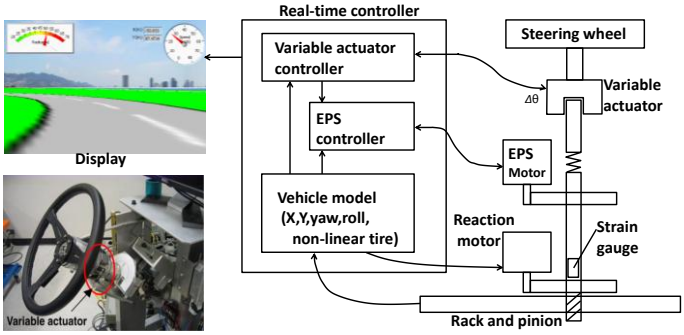

FIGURE 8. EXPERIMENTAL SETUP

In the normal EPS system in Fig. 9 (a), while the driver tries to maintain a constant steering-wheel angle, large oscillations in the steering torque were observed, due to changes in the gear ratio. On the other hand, Fig. 9(b) shows that the proposed controllers successfully reduced the oscillations and maintained the steering torque at approximately 3 Nm. However, we observe that small oscillations are still present in Fig. 9(b) and small unnaturalness was still felt by the driver, especially when changing the rotational direction of the variable-gear actuator.

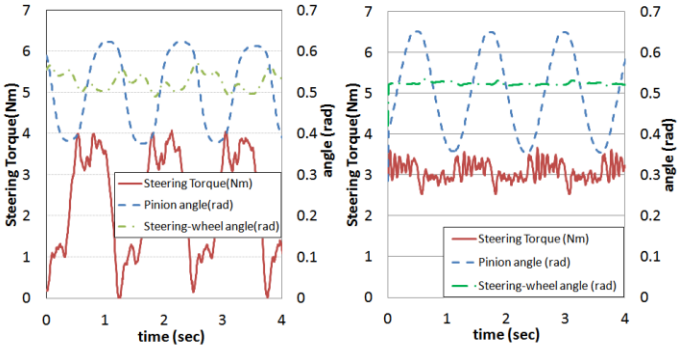

(a) normal EPS (b) with controller C_1, C_2

FIGURE 9 THE EFFECT OF C_1 AND C_2

Evaluation of steering feel with EPS assistive torque

In this subsection, the steering feel of the EPS system is evaluated in the HIL simulator for achieving the second desired condition. Fig. 10 shows the Lissajous plot of a sinusoidal operation for the gear ratio $\alpha = 1$. The shape of the plot in Fig. 10 matches the desired one, and the plot does not have sharp torque variations. This result suggests that controllers C_1 and C_2 provide good EPS assistive characteristics. But since small

torque oscillations are still present, the second desired condition is not completely achieved. Also, in this experiment the gear ratio, α, equals one, while the final goal is that the second desired condition is achieved when α is a function of the vehicle speed.

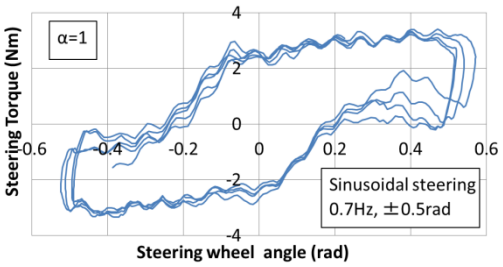

FIGURE 10. LISSAJOUS PLOT WITH C_1, C_2

FRICTION COMPENSATION AND NARROW-BAND DISTURBANCE REJECTION

From the experimental results shown above, the first two desired conditions have been mostly achieved but small residual unnatural torques and vibrations still exist as shown in Fig. 9(b) and Fig. 10. Controller C_1 is modified in this section to further improve the performance. To begin diagnosing the problem, an elemental experiment is performed as follows: first the variable actuator is deactivated, i.e. the steering wheel is disconnected from the steering shaft, and the reference steering speed is set as $V_{ref} = 0.78\sin(2\pi t)$. This reference velocity was applied as V_v in the feedback loop of Fig. 3. Fig. 11(a) shows the structure for the elemental experiment. Fig. 11(b) shows the result of velocity tracking performance. From the experimental result, we see that friction and velocity ripples greatly affect the tracking performance.

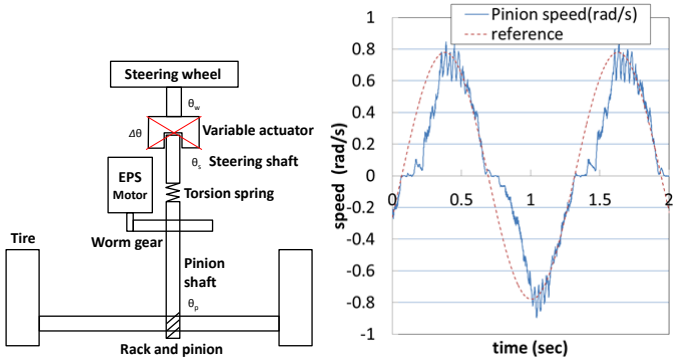

(a) structure of elemental experiment (b) velocity tracking

FIGURE 11. ELEMENTAL VELOCITY EXPERIMENT

In view of this experimental result, the control loop for C_1 is revised as shown in Fig. 12. The controller now considers the friction effects and contains a friction compensation block and a narrow-band disturbance observer for disturbance rejection.

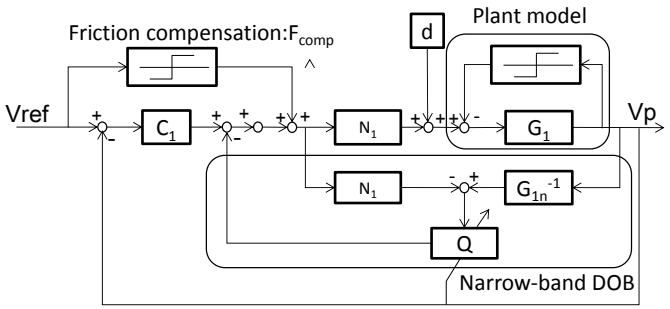

FIGURE 12. REVISED CONTROL STRUCTURE

Friction compensation

Friction exists at the pinion shaft due to the resistance of the worm gear and the preload of the rack and pinion. To improve the tracking performance, a Coulomb-friction compensation signal, F_{comp} is applied as follows [1]:

$$F_{comp} = T_f sat(V_f + \gamma T_{ext}(1 - |V_f|)) \\ V_f = \beta V_p,\ T_{ext} = T_e + T_k + T_{SAT\_est} \quad (4)$$

where T_f is the maximum value of the friction, β and γ are positive tuning parameters. sat(.) is the saturation function whose output is limited to between ±1. The compensator F_{comp} becomes a typical friction compensation scheme $T_f\,sgn(V_p)$ when the pinion-speed $|V_p|$ is large, and becomes a positive feedback of the external force $T_f\,sat(\gamma T_{ext})$, when the pinion speed V_p is zero. The latter construction is to compensate the static friction and initialize motion for the pinion shaft.

Fig. 13 shows the results with and without friction compensation. The tracking performance without friction compensation is particularly poor when the motor changes its rotation direction. On the other hand, the friction compensator greatly improves the tracking performance.

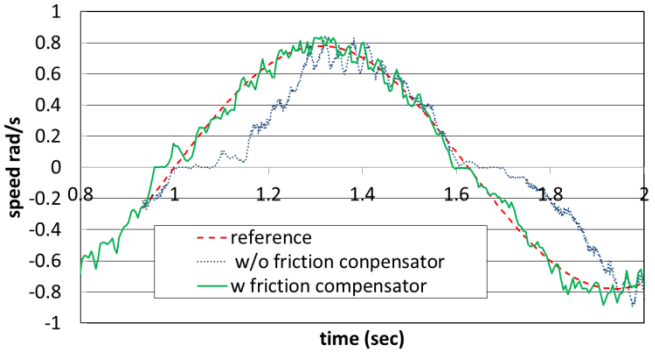

FIGURE 13. EFFECT OF FRICTION COMPENSATION

Narrow-band disturbance rejection

From Fig. 13 we observe that small-magnitude vibrations still exist after the friction compensation. To investigate the root

cause of the vibrations, we performed an elemental EPS motor experiment at a constant speed. Fig. 14 presents the obtained results, from which it is observed that the EPS motor contains a strong vibration component at 15 Hz when the normalized motor velocity is at 1 rad/sec.

Alternating the motor speed ω_m additionally reveals that the vibration frequency ω_v also changes according to $\omega_v = \gamma_n \omega_m$, where γ_n depends on the number of magnetic pairs in the motor.

We apply the narrow-band disturbance observer (DOB) [6] to cancel the harmonic vibrations in the system. One special property of the EPS system is that the plant contains a delay of 4 ms, which comes from the EPS driver N_1. Such a delay greatly affects the performance of disturbance rejection. This paper applies a new Q-filter design method [5] to improve the disturbance rejection.

Consider the block-diagram construction in Fig. 15. We have used the discussed result that N_1 is approximately a delay element z^{-m}. Computing the transfer function from d to V_p, gives the following z-domain relation

$$V_p(z^{-1}) = \frac{G_1(z^{-1})(1-z^{-m}Q(z^{-1}))d(z^{-1})}{1+z^{-m}G_1(z^{-1})C_1(z^{-1})+z^{-m}Q(z^{-1})[G_{1n}^{-1}(z^{-1})G_1(z^{-1})-1]} \quad (5)$$

The DOB design provides the disturbance cancellation property by incorporating the term $(1-z^{-m}Q(z^{-1}))d(z^{-1})$ in Eq. (5). Consider the following construction:

$$1-z^{-m}Q(z^{-1}) = F_{nf}(z^{-1})K(z^{-1}) \quad (6)$$

$$K(z^{-1}) = k_1 + k_2 z^{-1} + \cdots + k_{n_m+1} z^{-m} \quad (7)$$

$$F_{nf}(z^{-1}) = B_{nf}(z^{-1})/A_{nf}(z^{-1}) \quad (8)$$

$$B_{nf}(z^{-1}) = b_1 + b_2 z^{-1} + \cdots + b_{n_b+1} z^{-n_b} \quad (9)$$

$$A_{nf}(z^{-1}) = a_1 + a_2 z^{-1} + \cdots + a_{n_a+1} z^{-n_a} \quad (10)$$

where $F_{nf}(z^{-1})$ is a general notch-filter and $K(z^{-1})$ is a FIR filter.

Solving (6) gives

$$Q(z^{-1}) = z^m \frac{A_{nf}(z^{-1}) - B_{nf}(z^{-1})K(z^{-1})}{A_{nf}(z^{-1})} = z^m \frac{X(z^{-1})}{A_{nf}(z^{-1})} \quad (11)$$

Since z^m is not causal, to make $Q(z^{-1})$ realizable, the coefficients of z^{-i} need to be zero for $i = 0,1,2,\ldots,m-1$ in $X(z^{-1})$. This causality condition is obtained by

$$\begin{bmatrix} a_1 \\ a_2 \\ \vdots \\ a_m \end{bmatrix} - \begin{bmatrix} b_1 & 0 & 0 & 0 \\ b_2 & b_1 & 0 & 0 \\ \vdots & \ddots & \ddots & 0 \\ b_m & \ldots & b_2 & b_1 \end{bmatrix} \begin{bmatrix} k_1 \\ k_2 \\ \vdots \\ k_m \end{bmatrix} = 0 \quad (12)$$

For the EPS system, the 4-ms input delay and 1-ms sampling time give m=4 in the narrow-band DOB design. Using a standard notch-filter in the structure of Eq. (16), we can solve the above equations and obtain the Q filter in Eq. (13)

$$Q(z^{-1}) = \frac{-\beta_n{}^2 k_3 + 2\beta_n \cos\omega_v k_4 - \beta_n^2 k_4 z^{-1}}{1-2\alpha_n \cos\omega_v z^{-1} + \alpha_n^2 z^{-2}} \quad (13)$$

$$k_3 = \alpha_n^2 - \beta_n^2 + 2\beta_n \cos\omega_v k_2 \quad (14)$$

$$k_4 = -\beta_n^2 k_2 + 2\beta_n \cos\omega_v k_3 \quad (15)$$

$$k_1 = 1$$

$$k_2 = -2\cos\omega_v(\alpha_n - \beta_n)$$

$$F_{nf}(z^{-1}) = \frac{1-2\beta_n \cos\omega_v z^{-1} + \beta_n^2 z^{-2}}{1-2\alpha_n \cos\omega_v z^{-1} + \alpha_n^2 z^{-2}} \quad (16)$$

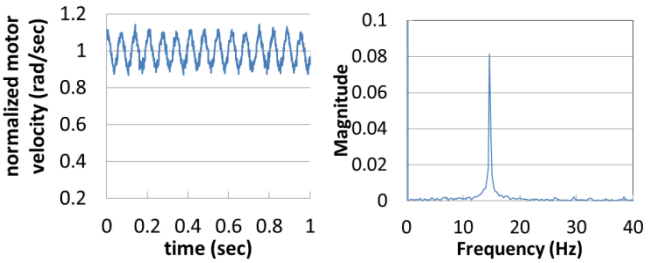

(a) constant velocity (b)FFT of constant velocity

FIGURE 14. ELEMENTAL MOTOR EXPERIMENT

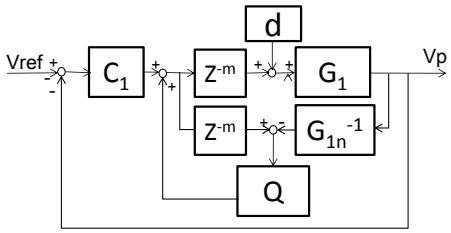

FIGURE 15. STRUCTURE OF NARROW-BAND DOB

Fig. 16 shows the effect of the Q filter, where we see that the added term $1-z^{-m}Q(z^{-1})$ has introduced small gains around a local frequency, which is not achievable using a standard band-pass filter. Fig. 17 shows the result of the elemental EPS motor experiment using the same configurations as those in Fig. 14. The original spectral peak at 15Hz is seen to have been removed.

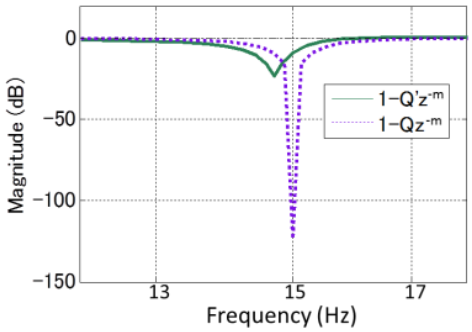

FIGURE 16. Q FILTER EFFECT: DASHED LINE—PROPOSED DESIGN; SOLID LINE—REGULAR BAND-PASS FILTER

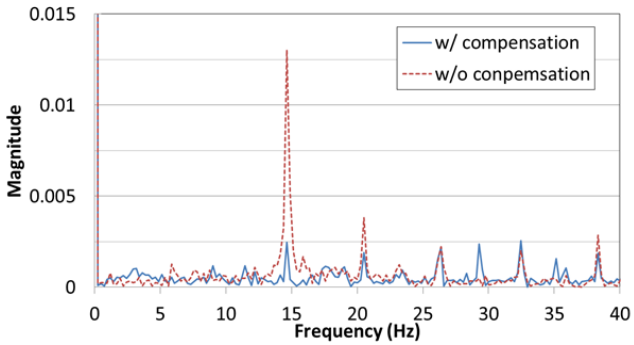

FIGURE 17. EFFECT OF NEW Q FILTER

The above are results under a constant EPS motor speed. Using the discussed relationship between the motor velocity and the vibration frequency $\omega_v = \gamma_n \omega_m$, we can make the Q filter adaptive to track the peak vibration frequencies under varying EPS motor speeds. Fig. 18 shows the compensation results. Comparing Fig. 18(a) and Fig. 18(b), we see that the algorithms provided significant performance enhancement.

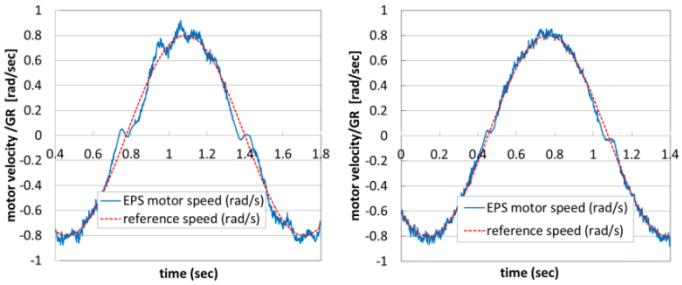

(a) without DOB (b) with proposed DOB

FIGURE 18. TRACKING PERFORMANCE

EXPERIMENTAL RESULT OF THE REVISED CONTROLLERS

The revised control system which combines controllers C_1, C_2, C_3 with the friction compensator and narrow-band disturbance rejection are evaluated in this section.

The result of the steering torque with variable gear ratio is shown Fig. 19(a). The torque oscillation has been reduced compared to the result of the first attempt in Fig. 9(b). In particular, the torque variations caused by the changes of the rotational direction of variable motor is significantly reduced. Fig. 19(b) shows the result of the Lissajous plot under sinusoidal steering wheel motions when the gear ratio, α, is 1. The torque vibration is also significantly reduced compared to the results in Fig. 10.

Fig. 20 shows the result of the Lissajous plot under sinusoidal steering wheel motions with a time-varying gear ratio. The gear ratio change is also sinusoidal and is given by $\alpha = 1 + 0.3\sin(2.2\pi t)$. Fig. 20(a) shows the uncompensated result. The plot does not repeatedly follow a hysteresis curve and the driver feels significant feedback torque differences in each sinusoidal period. On the other hand, Fig. 20(b) shows the results using the revised controllers. Unlike the results in Fig. 20(a), the plot in Fig. 20(b) repeatedly follows a single hysteresis curve. As a result, the revised controllers are able to cancel the unnatural EPS torque and maintain normal EPS characteristics.

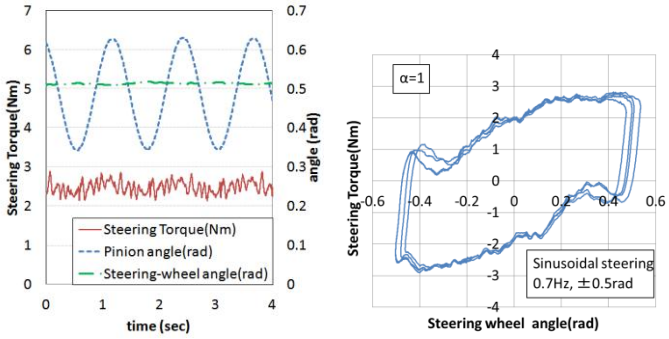

(a) torque vibration (b) Lissajous plot

FIGURE 19. EFFECT OF REVISED CONTROL

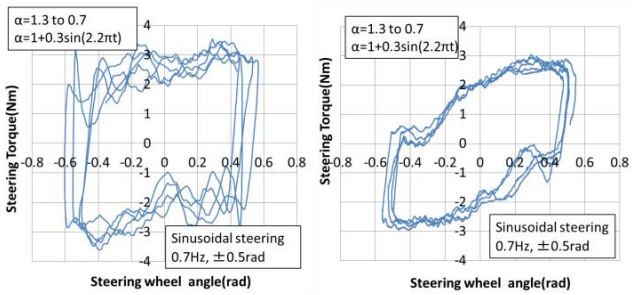

(a) original EPS controller (b) revised controller

FIGURE 20. LISSAJOUS PLOT

Fig. 21 shows the result of the Lissajous plot under sinusoidal steering wheel motions subjected to different road friction coefficients (μ is set to three different test conditions $\mu = 0.5,1,1.5$) where the gear ratio $\alpha = 1$. The experiment evaluates the third desired condition. Fig. 21(a) shows the result of normal EPS control. It can be seen that the steering differed under different road friction coefficients. More specifically, smaller torque was needed under smaller road friction coefficients and larger torque was needed under larger coefficients. Note that this torque difference transmits the road condition to the driver. Fig. 21(b) shows the result of revised system but without C_3. In this case, the driver did not feel significant steering difference under different road conditions, which indicate that the controllers rejected/cancelled the road information. Fig. 21(c) shows the result of revised system with C_3. We observe that the steering torque varies under different road conditions, indicating the road information is transmitted back to the driver.

The experimental results show that the revised controllers are able to satisfy the three desired conditions.

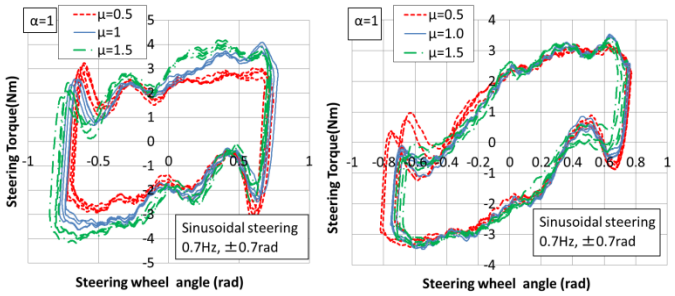

(a) normal EPS (b) revised system without C_3

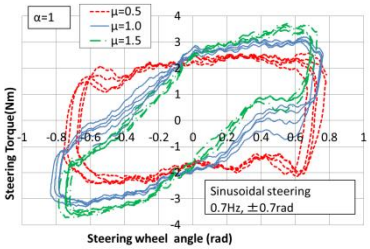

(c) revised system with C_3

FIGURE 21. LISSAJOUS PLOT (EVALUATE C_3)

STABILITY AND ROBUSTNESS

The controllers need to satisfy not only nominal stability but also robust stability, since plant uncertainties always exist in practice. The combined closed loop including C_1, C_2, C_3 and the narrow-band DOB is shown in Fig. 22, where N_1 is the time delay of the EPS driver, N_2 is the time delay of the tire sensor. Additionally, $V_{mn'} = V_{mn}/s$; d_R is the road information; and d_{inn} is the disturbance generated in the inner model. The friction compensator is not included in Fig. 22 since it does not affect the stability. When there is no model uncertainty, the closed loop is simplified to Fig. 23, where $G_2 = G_1 G_2'$. When there are model mismatches, the closed loop changes to Fig. 24. We discuss the stability in two parts:

Nominal model stability

The stability condition for the nominal system in Fig. 23 is that the poles of feedback loops of V_p, and $-T_k$ are stable. Since QN_1 and C_3N_2 are stable, we need the roots of the closed-loop characteristic polynomial, i.e., $1 + C_1G_1N_1 + C_1C_2G_2N_1 = 0$, to be stable.

Robust stability

The model uncertainty is assumed to be in the following standard multiplicative form

$$\widetilde{G}_i(s) = \big(1 + \Delta_i(s)W_i(s)\big)G_i(s),\ |\Delta_i(j\omega)| \le 1,\ \forall\omega, i = 1,2,3 \quad (17)$$

where $W_i(s)$'s are weight functions, $\Delta_i(j\omega)$'s are the perturbations. Fig. 24 can be transformed to the generalized representation in Fig. 25, where M(s) can be shown to be given by Eq. (18).

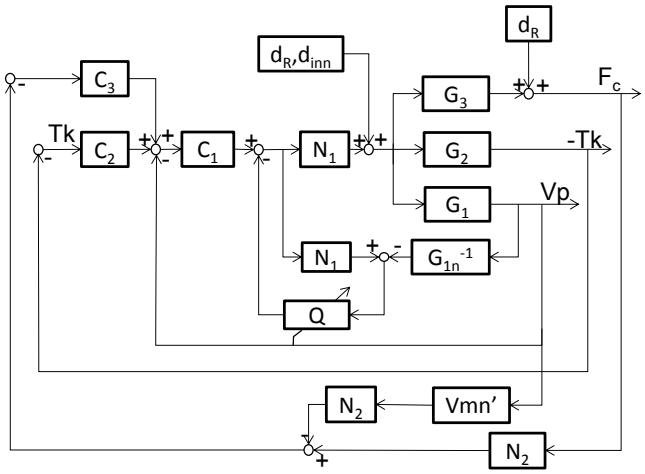

FIGURE 22. FEEDBACK SYSTEM BLOCK DIAGRAM

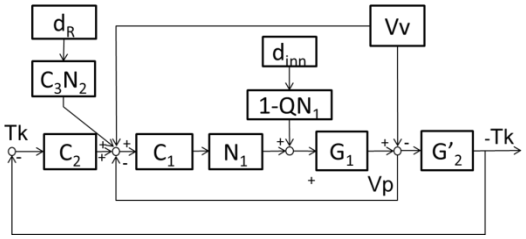

FIGURE 23. SIMPLIFIED BLOCK DIAGRAM

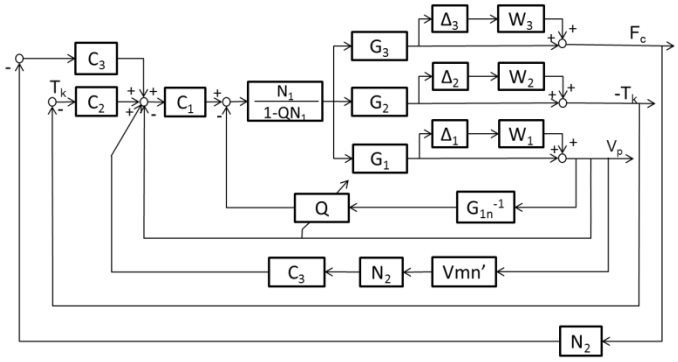

FIGURE 24. THE SYSTEM ICLUDING MODEL UNCERTAINTY

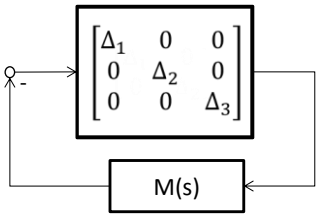

FIGURE 25. THE GENERALIZED BLOCK DIAGRAM OF FIG.24

$$M = N\begin{bmatrix} (C_1G_1 - C_1C_3G_1V_{mn},N_2 + Q)w_1 & C_1C_2G_1w_2 & C_1C_3G_1N_2w_3 \\ \left(C_1G_2 - C_1C_3G_2V_{mn},N_2 + \frac{G_2}{G_1}Q\right)w_1 & C_1C_2G_2w_2 & C_1C_3G_2N_2w_3 \\ \left(C_1G_3 - C_1C_3G_3V_{mn},N_2 + \frac{G_3}{G_1}Q\right)w_1 & C_1C_2G_3w_2 & C_1C_3G_3N_2w_3 \end{bmatrix} \quad (18)$$

$$N = \frac{N_1}{1 + C_1G_1N_1 + C_1C_2G_2N_1}$$

The μ-analysis tool can be applied to derive the robust stability condition [5]. The closed-loop system in Fig. 25 is stable if and only if the structured singular value of M(s) is strictly less than 1. The structured singular value of M(s), denoted as $\mu_\Delta(M)$, is calculated as follows (See Appendix for details):

$$\begin{aligned} &\mu_\Delta(M) = |P_1| + |P_2| + |P_3| \\ &P_1 = N(C_1G_1 - C_1C_3G_3V_{mn},N_2 + Q)W_1 \\ &P_2 = NC_1C_2G_2W_2\ ,\ P_3 = NC_1C_3G_3N_2W_3 \\ &N = N_1/(1 + C_1G_1N_1 + C_1C_2G_2N_1) \end{aligned} \quad (19)$$

Fig. 26 shows the values of the structured singular value μ_Δ, where we assumed a 10% model uncertainty. It can be observed that the structured singular value is strictly less than 1. Hence the system is robustly stable.

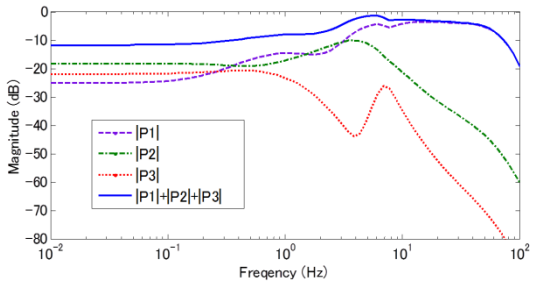

FIGURE 26. STRUCTURED SINGULAR VALUE

CONCLUSION

In this paper we have discussed the problem of mitigating unnatural torque in variable-gear-ratio systems. Three controllers C_1, C_2, C_3 were proposed to achieve the desired objectives. We have observed that the three controllers by themselves were not sufficient to provide satisfactory system performance. In response, we then presented a friction compensation and narrow-band disturbance rejection scheme to improve the system. Experimental results show that the revised control scheme was effective and provided satisfactory performance. Robust stability under the model uncertainty was evaluated by structured singular value analysis.

REFERENCES

[1] Sugita, S., Tomizuka, M., 2010, "Cancellation of Unnatural Reaction Torque in Variable-Gear-Ratio", Journal of Dynamic Systems, Measurement, and Control, 134, 021019 (2012), DOI:10.1115/1.4004577

[2] Morita, Y., Torii, K., Tsuchida, N., Iwasaki, M., Ukai, H., Matsui, N., Hayashi, T., Ido, N., Ishikawa, H., 2008, "Improvement of Steering Feel of Electric Power Steering System With Variable Gear Transmission System Using Decoupling Control," IEEJ Trans. Electron., Inf. Syst., 129(12), pp. 2136–2143.

[3] Minaki, R., Hoshino, H., and Hori, Y., 2009, "Ergonomic Verification of Reactive Torque Control Based on Driver's Sensitivity Characteristics for Active Front Steering," Vehicle Power and Propulsion Conference, IEEE. pp.160-164, 7-10 Sept. 2009.

[4] Takizawa, T., Yanagisawa, T., Ono, K., and Sakatani, I., "Load measuring device for rolling bearing unit and load measuring rolling bearing unit," U.S. Patent 7 320 257, Jan. 22, 2008.

[5] Chen, X., and Tomizuka, M., 2012, " Decoupled Disturbance Observers for Dual-input-single-output Systems with Application to Vibration Rejection in Dual-stage Hard Disk Drives," in Proceedings of 2012 ASME Dynamic Systems and Control Conference, and 2012 Motion & Vibration Conference, Ft. Lauderdale, FL, Oct. 17-19, 2012, pp. 1544-1554.

[6] Chen, X., and Tomizuka, M., "A Minimum Parameter Adaptive Approach for Rejecting Multiple Narrow-Band Disturbances with Application to Hard Disk Drives," IEEE Transactions on Control Systems Technology, vol. 20, no. 2, pp. 408-415, Mar. 2012.

[7] H. Pacejka, E. Bakker, and L. Nyborg, "Tyre modeling for use in vehicle dynamic studies," 1987, SAE Tech. Paper 870 421.

[8] Y. H. J. Hsu, S. Laws, C. D. Gadda, and J. C. Gerdes, "A method to estimate the friction coefficient and tire slip angle using steering torque," presented at the ASME Int. Mechan. Eng. Congr. Expo. (IMECE), Chicago, IL, 2006.

[9] Mammer, S., and Koenig, D., 2002, "Vehicle Handling Improvement by Active Steering, Vehicle System Dynamics," Veh. Syst. Dyn., 38(3), pp. 211–242.

[10] Sienel, W., 2002, "Robust Decoupling for Active Car Steering Holds for Arbitrary Dynamic Tire Characteristics," IEE Proceedings - Control Theory and Applications, 149(5), p. 394.

[11] Packard, A., and Doyle, J., "The complex structured singular value," Automatica, vol. 29, no. 1, pp. 71–109, 1993.

APPENDIX A: STRUCTURED SINGULAR VALUE

For Fig. 25, the structured singular value is [11]:

$$\mu_\Delta(M) = \frac{1}{min\{\bar{\sigma}(\Delta):\Delta\in\Delta, det(I+M\Delta)=0\}} \quad (20)$$

where the denominator is the maximum singular value of the smallest (in the sense of H_∞ norm) perturbation Δ that reaches the stability boundary

The matrix M in Eq.(19) is

$$\mathrm{M}=\begin{bmatrix} P_1 & \widehat{d_1}P_1 & \widehat{d_2}P_1 \\ \frac{1}{\widehat{d_1}}P_2 & P_2 & \widehat{d_3}P_2 \\ \frac{1}{\widehat{d_2}}P_3 & \frac{1}{\widehat{d_3}}P_3 & P_3 \end{bmatrix} \tag{21}$$

where $\widehat{d_1}=\frac{C_1C_2G_1W_2}{(C_1G_1-C_1C_3G_3V_{nm}N_2+Q)W_1}$, $\widehat{d_2}=\frac{C_1C_3G_1N_2W_3}{(C_1G_1-C_1C_3G_3V_{nm}N_2+Q)W_1}$,$\widehat{d_3}=\frac{C_3N_2W_3}{C_2W_2}$

We define $\mathrm{D}=\{diag[d_1,d_2,d_3]\}$, $\widehat{d_1}=d_1/d_2$, $\widehat{d_2}=d_1/d_3$, $\widehat{d_3}=d_2/d_3$, $\mathrm{M}'=\begin{bmatrix} P_1 & P_1 & P_1 \\ P_2 & P_2 & P_2 \\ P_3 & P_3 & P_3 \end{bmatrix}$, i.e. $\mathrm{M}=\mathrm{DM}'D^{-1}$.

Using the determinant identity det(I+AB)=det(I+BA) gives

$$\det(\mathrm{I}+\mathrm{M}'\Delta)=\det(\mathrm{I}+\mathrm{M}'D^{-1}\Delta D)=\det(\mathrm{I}+\mathrm{DM}'D^{-1}\Delta)$$

Then

$$\mu_\Delta(M)=\mu_\Delta(DM'D^{-1})=\mu_\Delta(M')=\mu_\Delta\begin{bmatrix} P_1 & P_1 & P_1 \\ P_2 & P_2 & P_2 \\ P_3 & P_3 & P_3 \end{bmatrix} \tag{22}$$

Furthermore,

$$\mathrm{M}'\Delta=\begin{bmatrix} P_1 & P_1 & P_1 \\ P_2 & P_2 & P_2 \\ P_3 & P_3 & P_3 \end{bmatrix}\begin{bmatrix} \Delta_1 & 0 & 0 \\ 0 & \Delta_2 & 0 \\ 0 & 0 & \Delta_3 \end{bmatrix}=\begin{bmatrix} P_1 \\ P_2 \\ P_3 \end{bmatrix}\begin{bmatrix} \Delta_1 & \Delta_2 & \Delta_3 \end{bmatrix} \tag{23}$$

$$\Delta\mathrm{M}'=\begin{bmatrix} \Delta_1 & \Delta_2 & \Delta_3 \end{bmatrix}\begin{bmatrix} P_1 \\ P_2 \\ P_3 \end{bmatrix}=P_1\Delta_1+P_2\Delta_2+P_3\Delta_3 \tag{24}$$

Using Eqs. (23-24), we have

$$det(I+M'\Delta)=det(I+\Delta M')=1+P_1\Delta_1+P_2\Delta_2+P_3\Delta_3 \tag{25}$$

Combining (23) and (20), the minimum- H_∞ -norm perturbation is obtained if $|\Delta_1|=|\Delta_2|=|\Delta_3|=|\Delta_0|$ and the following equality holds.

$$1-|P_1||\Delta_1|-|P_2||\Delta_2|-|P_3||\Delta_3|=0 \tag{26}$$

From Eq. (20), (22), (26), the structured singular value is

$$\mu_\Delta(M)=\frac{1}{|\Delta_0|}=|P_1|+|P_2|+|P_3| \tag{27}$$